Convergent thermal conductivity in strained monolayer graphene

Guotai Li,[1,2] Jialin Tang,[2,3] Jiongzhi Zheng,[4] Qi Wang,[2] Zheng Cui,[1,2] Ke Xu,[5] Jianbin Xu,[5] Te-Huan Liu,[6,*] Guimei Zhu,[7,†] Ruiqiang Guo,[2,‡] and Baowen Li[8,7]

[1]*Institute of Thermal Science and Technology, Shandong University, Jinan, Shandong 250061, China*
[2]*Thermal Science Research Center, Shandong Institute of Advanced Technology, Jinan, Shandong 250103, China*
[3]*Institute of Advanced Technology, Shandong University, Jinan, Shandong 250061, China*
[4]*Thayer School of Engineering, Dartmouth College, Hanover, New Hampshire 03755, USA*
[5]*Department of Electronic Engineering and Materials Science and Technology Research Center, The Chinese University of Hong Kong, Shatin, N.T., Hong Kong SAR 999077, China*
[6]*School of Energy and Power Engineering, Huazhong University of Science and Technology, Wuhan, Hubei 430074, China*
[7]*School of Microelectronics, Southern University of Science and Technology, Shenzhen, Guangdong 518055, China*
[8]*Department of Materials Science and Engineering, Department of Physics, Southern University of Science and Technology, Shenzhen, Guangdong 518055, China and Shenzhen International Quantum Academy, Shenzhen 518048, China*

(Received 9 November 2023; revised 17 December 2023; accepted 19 December 2023; published 17 January 2024)

The strain dependence of thermal conductivity (κ) in monolayer graphene, with reports of enhancement, suppression, or even divergence, has been highly controversial. To address this open question, we have systematically investigated the effects of tensile strain on the κ of graphene using the exact solution of the Peierls-Boltzmann transport equation based on the *first-principles* interatomic force constants combined with machine learning assisted molecular dynamics simulations. In contrast to previous studies, we find that the κ in the strained graphene is convergent after considering four-phonon scattering, which is dominant for the long-wavelength flexural phonons because of its much weaker frequency dependence ($\tau_4^{-1} \propto \omega^\beta$ with $\beta < 2$) compared to the three-phonon scattering case ($\tau_3^{-1} \propto \omega^\beta$ with $\beta > 2$). Furthermore, κ exhibits nonmonotonic variations with increasing strain up to 8% due to the competition between phonon lifetime, group velocity, and heat capacity of acoustic phonons. Our results deepen the fundamental understanding of thermal transport in strained graphene and offer insights for tuning the thermal properties of two-dimensional materials through strain engineering.

DOI: 10.1103/PhysRevB.109.035420

I. INTRODUCTION

Strain engineering is a powerful approach to manipulating thermal properties [1–3]. Strain changes atomic structures and bonding strength, thereby greatly affecting the lattice vibrations and thermal properties of materials. Substantial red shifts of the 2D and G bands have been observed in monolayer graphene under tensile strain [4]. Remarkable enhancement in thermal conductivity (κ) caused by strain has been reported in polymers [5,6], semiconductors [7,8], and other materials [9–12]. Particularly, the stretching-induced restructuring of polymer chains can result in orders of magnitude increases in the κ of polymers, from a typical value of around 0.1 W m^{-1} K^{-1} to a very high κ of approximately 104 W m^{-1} K^{-1}, as the fiber quality approaches "ideal" single crystals [5]. By applying a ~9% cross-plane compressive strain, the cross-plane κ of bulk MoS_2 increases from 3.5 to about 25 W m^{-1} K^{-1} mainly due to the substantially strengthened interlayer force and the resulting modification of the phonon dispersion along the cross-plane direction [8]. Strain can also induce anomalous thermal behaviors, as observed in cases like cubic boron arsenide [7], where a nonmonotonic pressure-dependent κ is attributed to the competition between three- and four-phonon scattering processes originating from its unique phonon band structure.

Recent studies have demonstrated that strain can largely affect the κ of monolayer graphene [13–16], a two-dimensional material that has attracted great interest for both fundamental research and practical applications in recent years due to its extraordinary mechanical [17], electronic [18], and thermal properties [19,20]. Notably, the κ of graphene, which falls in the range of 2000–5000 W m^{-1} K^{-1}, is considered the highest among all known materials [21–23], offering great promise for achieving efficient heat dissipation in electronics and optoelectronics [24].

Previous experimental works have shown that strain can strongly suppress the κ of monolayer graphene. For instance, under a 0.12% biaxial tensile strain, the κ of suspended monolayer graphene drops by approximately 20% at 350 K [25]. On the other hand, the κ of multilayer graphene exhibits a drastic reduction of 60%–70% from the total by applying a strain of

*thliu@hust.edu.cn
†zhugm@sustech.edu.cn
‡ruiqiang.guo@iat.cn

approximately 0.1% [26]. On the simulation side, the impact of strain on graphene's κ has been the subject of significant debate, varying according to different calculation methods. Employing molecular dynamics (MD) simulations, Li *et al.* reported that the κ of monolayer graphene decreases monotonically with increasing tensile strain [27]. Using an iterative approach to solve the Peierls-Boltzmann transport equation (PBTE) based on the *first-principles* calculation, a reduction of κ due to a 1% tensile strain was also reported in monolayer graphene with a sample diameter of 10 μm [28], which is mainly caused by boundary scattering of long-wavelength phonons. In contrast, using the same approach, Fugallo *et al.* showed that a 4% isotropic tensile strain increases the κ of monolayer graphene by about 20% at room temperature [29].

Beyond these observations, a more important question pertains to whether the κ of strained graphene converges with system size. In 2001, Klemens [30] pointed out that the κ of graphene diverges logarithmically with system size using a model [31] when only considering the contribution of the transverse (TA) and longitudinal acoustic (LA) phonons. However, Klemens' model overlooks the role of flexural modes (ZA), which have a crucial influence on the phonon scattering channels and thermal conductivity of graphene [32,33]. Nevertheless, the divergence of κ in strained graphene has received support from several subsequent studies, including classical MD simulations and *ab initio* PBTE calculations based on the single-mode relaxation time approximation (RTA) and the full iterative approach [13–16]. Confirmation of the convergence of κ in strained graphene requires further investigation because of two major reasons. First, the phonon population in MD simulations follows the Maxwell-Boltzmann distribution and thus any quantum effect is disregarded. Second, the PBTE calculations considered only the three-phonon processes. The inclusion of four-phonon scattering in PBTE calculations may change the convergence behavior of κ in strained graphene. Recent research has reported that the κ of unstrained graphene was significantly reduced by four-phonon scattering [34] because the reflection symmetry selection rule (RSSR) forbids three-ZA processes while allowing four-ZA scattering. Gu *et al.* later confirmed the substantial drop in graphene's κ due to four-phonon scattering by additionally considering temperature-dependent interatomic force constants (IFCs) [35]. Considering the pronounced impact of four-phonon scattering on the κ of pristine graphene, it is anticipated that four-phonon scattering plays a vital role in determining the phonon scattering landscape and, consequently, the convergence of κ in strained graphene.

In this work, we have revisited the κ of graphene under tensile strain using PBTE based on first-principles calculation and machine learning assisted molecular dynamics simulations, demonstrating that the κ of the strained graphene is convergent after further considering the four-phonon scattering in addition to the three-phonon scattering. This is mainly because the scattering rates of long-wavelength ZA phonons are dominated by four-phonon scattering, which exhibits a much weaker frequency dependence of $\omega^{\beta}(\beta < 2)$ as compared to $\omega^{\beta}(\beta > 2)$ for three-phonon scattering.

In addition, we predict a nonmonotonic variation of κ of graphene in the strain range $0 \leqslant \varepsilon \leqslant 8\%$, which can be attributed to the increase of the phonon lifetime and group velocity of ZA phonons for $\varepsilon \leqslant 4\%$ and the reduction of heat capacity and phonon lifetime of TA and LA phonons for $\varepsilon \geqslant 6\%$ as strain increases. Our results enrich and deepen the fundamental understanding of phononic thermal transport in strained graphene and will shed light on heat conduction tuning of two-dimensional (2D) materials.

II. COMPUTATIONAL METHODS

A. Thermal conductivity calculation

The lattice thermal conductivity can be calculated within the framework of the PBTE [36,37]. The PBTE is solved for the nonequilibrium phonon distribution function resulting from an applied small temperature gradient, ∇T. By keeping only the terms linear in ∇T, for a given mode λ, one can obtain the deviation from equilibrium for its phonon distribution, i.e., $n_\lambda = n_\lambda^0 - \boldsymbol{F}_\lambda \cdot \nabla T dn_\lambda^0/dT$, where $\boldsymbol{F}_\lambda = \tau_\lambda^0(\boldsymbol{v}_\lambda + \boldsymbol{\Delta}_\lambda)$ [38], τ_λ^0 is the phonon relaxation time obtained from RTA, n_λ^0 is the Bose-Einstein distribution, $\boldsymbol{v}_\lambda$ is the phonon group velocity, and $\boldsymbol{\Delta}$ is the linear functional of $\boldsymbol{F}_\lambda$. $\boldsymbol{\Delta} \equiv 0$ corresponds to the results obtained from RTA. From this, the thermal conductivity can be linearized and solved iteratively using τ_λ^0 obtained from RTA as a starting guess. The κ along the transport direction can be calculated as the sum of contribution over all the phonon modes λ:

$$\kappa^{\alpha\beta} = \frac{1}{k_B T^2 \Omega N} \sum_\lambda (\hbar\omega_\lambda)^2 n_\lambda^0 \big(n_\lambda^0 + 1\big) v_\lambda^\alpha F_\lambda^\beta, \tag{1}$$

where α and β denote Cartesian directions, $k_{\rm B}$ is the Boltzmann constant, Ω is the volume of the unit cell, N is the total number of $\mathbf{q}$ points, $\hbar$ is the reduced Plank constant, and ω_λ is the phonon frequency. The total relaxation time τ_λ^0 within the RTA framework is computed from Matthiessen's rule:

$$1/\tau_\lambda^0 = 1/\tau_\lambda^{\rm 3ph} + 1/\tau_\lambda^{\rm 4ph} + 1/\tau_\lambda^{\rm iso}. \tag{2}$$

where $1/\tau_\lambda^{\rm 3ph}$ is the three-phonon (3ph) scattering rate, $1/\tau_\lambda^{\rm 4ph}$ is the four-phonon (4ph) scattering rate, and $1/\tau_\lambda^{\rm iso}$ is the phonon-isotope scattering rate.

B. First-principles computational details

All first-principles calculations were performed based on density functional theory (DFT) [39], as implemented in the Vienna *ab initio* simulation package (VASP) [40] with the projected augmented wave method [41]. The local density approximation (LDA) [42] was used for the exchange-correlation functional. For each structure, the unit cell was optimized using a cutoff energy of 600 eV and a k-point mesh of $21 \times 21 \times 1$, with a convergence criterion of 10^{-8} eV and 10^{-6} eV Å^{-1} for energy and Hellmann-Feynman force, respectively. The optimized lattice constant is 2.45 Å for the pristine graphene, which agrees well with the previous calculations [16,34]. The tensile strain is defined as $\varepsilon = (a - a_0)/a_0 \times 100\%$, where a and a_0 are the lattice constants of the strained and unstrained graphene, respectively. Based on the optimized crystal structures, the second-, third-, and fourth-order IFCs were calculated based on an $8 \times 8 \times 1$ supercell using the finite displacement method as implemented in PHONOPY [43], THIRDORDER.PY [38], and FOURTHORDER.PY

[44], respectively. Specifically, the interaction distance was restricted to ninth- and third-nearest neighbors for calculating the third- and fourth-order IFCs, respectively. Then we calculated the three-phonon, four-phonon, and phonon-isotope scattering rates based on the obtained IFCs. Finally, the thermal conductivity was calculated using our in-house modified version of the SHENGBTE code [38,44]. Because our study focuses on the effect of tensile strain on the thermal conductivity of monolayer graphene, we used zero-K interatomic force constants directly extracted from first-principles calculations and ignored the phonon renormalization effect [45–48].

We calculated the thermal conductivity using three different levels of approach with increasing accuracy: (I) RTA for both 3ph and 4ph; (II) iterative scheme for 3ph while RTA for 4ph; (III) full iterative scheme for both 3ph and 4ph. For the approach of level I, the κ was calculated using Matthiessen's rule by adding up all types of scattering rates. In the case of the 3ph iteration + 4ph RTA approach, the κ was obtained through an iterative scheme involving three-phonon scattering only, while the phonon-isotope and four-phonon scattering were treated at the RTA level. For the full iterative approach, the κ was determined through an iterative scheme considering three-phonon, four-phonon, and phonon-isotope scattering.

C. Estimation of $\kappa_{3+4}^{\mathrm{ZA}}$ in the long-wavelength limit

To estimate the $\kappa_{3+4}^{\mathrm{ZA}}$ corresponding to a larger **q**-point mesh under the RTA level, we first estimated the lifetime of phonons below 1 THz by fitting to the frequency dependence of each scattering term, and then calculated the $\kappa_{3+4}^{\mathrm{ZA}}$ contributed by modes below 1 THz, with all the other inputs obtained from SHENGBTE. We got the $\kappa_{3+4}^{\mathrm{ZA}}$ by summing up the result below 1 THz and that above 1 THz calculated using a $60 \times 60 \times 1$ **q**-point mesh. As the **q**-point mesh increases to $N = 3000$, the $\kappa_{3+4}^{\mathrm{ZA}}$ almost saturates within the considered strain range; e.g., for $\varepsilon = 2\%$, $\kappa_{3+4}^{\mathrm{ZA}}$ for $N = 3000$ is only 0.06% larger than that for $N = 2000$ at 300 K. We next further evaluate the contribution of $\kappa_{3+4}^{\mathrm{ZA}}$ by the phonons in the long-wavelength limit. Specifically, we define the minimum frequency corresponding to the **q**-point mesh density $N = 3000$ as the cutoff frequency ω_{cut} and calculated the contribution of $\kappa_{3+4}^{\mathrm{ZA}}$ by phonons below ω_{cut} by Eq. (5). The total thermal conductivity of ZA phonons in the long-wavelength limit $\kappa_{3+4}^{\mathrm{ZA},\infty}$ was then obtained by summing up the integral result below ω_{cut} and that above ω_{cut} calculated using a $3000 \times 3000 \times 1$ **q**-point mesh.

In this study, the thermal conductivity below a cutoff frequency ω_{cut} is calculated by

$$\kappa = \int_0^{\omega_{\mathrm{cut}}} \kappa_\omega g(\omega) d\omega, \tag{3}$$

where κ_ω is the thermal conductivity contributed by phonons with frequency ω, $g(\omega)$ is the phonon density of the states. Because the dispersion of the low-frequency ZA becomes linearized due to tensile strain, the total phonon density of the states at low frequency can be expressed as

$$g(\omega) = A\omega, \tag{4}$$

where A is a constant obtained by fitting the total phonon density of states at low frequency.

Applying Eqs. (3) and (4) to the ZA phonon branch, the κ contributed by ZA modes below ω_{cut} can be written as

$$\kappa^{\mathrm{ZA}} = \frac{1}{2\Omega} \int_0^{\omega_{\mathrm{cut}}} \frac{k_B(\hbar\omega/k_{\mathrm{B}}T)^2\, e^{\hbar\omega/k_{\mathrm{B}}T}}{(e^{\hbar\omega/k_{\mathrm{B}}T} - 1)^2} \tau \times \left[1 \Big/ \left(\frac{1}{\nu_{\mathrm{ZA}}^2} + \frac{1}{\nu_{\mathrm{TA}}^2} + \frac{1}{\nu_{\mathrm{LA}}^2} \right) \right] A\omega d\omega, \tag{5}$$

where τ was calculated using Matthiessen's rule considering $1/\tau^{3\mathrm{ph}}$, $1/\tau^{4\mathrm{ph}}$, and $1/\tau^{\mathrm{iso}}$, which were obtained from the fitting frequency dependence of three-phonon, four-phonon, and phonon-isotope scattering rates below 2 THz. ν_{ZA}, ν_{TA}, and ν_{LA} represent the sound velocity of the ZA, TA, and LA phonons, respectively. $\omega_{\mathrm{cut}} = 0.005, 0.007, 0.008$ THz was used for $\varepsilon = 2\%$, 4%, and 6%, respectively.

D. Molecular dynamics simulations

We determined the thermal conductivity by employing the homogeneous nonequilibrium molecular dynamics (HNEMD) [49,50]. This method applies an external force to each atom to perturb the system from equilibrium. The external force, $\boldsymbol{F}_i^{\mathrm{ext}}$, is expressed as a function of the per-atom energy E_i and the virial tensor $\mathbf{W}_i$:

$$\boldsymbol{F}_i^{\mathrm{ext}} = E_i \boldsymbol{F}_{\mathrm{e}} + \boldsymbol{F}_{\mathrm{e}} \cdot \mathbf{W}_i. \tag{6}$$

When the parameter $\boldsymbol{F}_{\mathrm{e}}$ (dimensionally an inverse length) is sufficiently small, the system remains within the linear-response regime, whereby a nonequilibrium heat current $\langle \boldsymbol{J} \rangle_{\mathrm{ne}}$, proportional to $\boldsymbol{F}_{\mathrm{e}}$, is generated. The proportionality can be delineated by

$$\frac{\langle J^\mu(t) \rangle_{\mathrm{ne}}}{TV} = \sum_\nu \kappa^{\mu\nu}(t) F_e^\nu, \tag{7}$$

where T represents the system's temperature, V denotes its volume, and $\kappa^{\mu\nu}$ is the thermal conductivity tensor. The heat current $\boldsymbol{J}$ for a system described by a many-body potential is defined as [51]

$$\boldsymbol{J} = \sum_i \boldsymbol{v}_i E_i + \sum_i \sum_{j \neq i} \boldsymbol{r}_{ij} \left(\frac{\partial U_j}{\partial \boldsymbol{r}_{ji}} \cdot \boldsymbol{v}_i \right), \tag{8}$$

where $\boldsymbol{r}_{ij} = \boldsymbol{r}_j - \boldsymbol{r}_i$, $\boldsymbol{r}_i$ is the position of particle i, and U is the potential energy. Given the hexagonal symmetry of the system, the in-plane heat transport within graphene is rendered isotropic. Consequently, the in-plane thermal conductivity tensor reduces to a scalar κ, which can be expressed as

$$\kappa(t) = \frac{\langle J(t) \rangle_{\mathrm{ne}}}{TVF_e}. \tag{9}$$

For computational efficiency, $\kappa(t)$ is recalculated as a time-cumulative average:

$$\kappa(t) = \frac{1}{t} \int_0^t \frac{\langle J(s) \rangle_{\mathrm{ne}}}{TVF_{\mathrm{e}}} ds \tag{10}$$

More technical and theoretical details about the HNEMD method can be found in Ref. [50].

Here, the HNEMD simulations were executed in two primary stages. First, the system was equilibrated for 0.4 ns within the canonical ensemble (*NVT*: constant number of

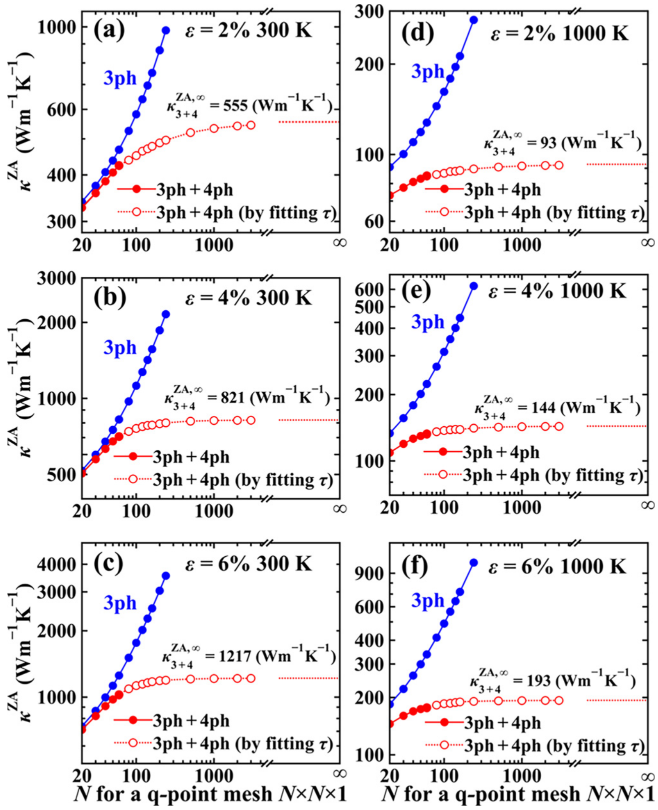

FIG. 1. Convergence of κ contributed by ZA phonons with respect to the size of **q**-point mesh ($N\times N\times 1$) for graphene with 2% (a), 4% (b), and 6% (c) isotropic tensile strain under RTA at 300 K, respectively. (d), (e), (f) are the same as (a), (b), (c), respectively, but for 1000 K.

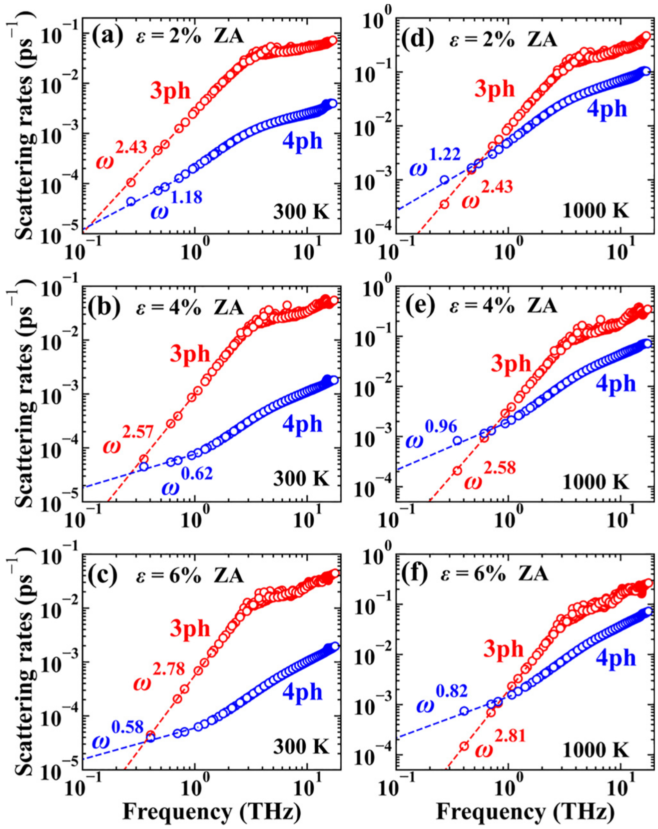

FIG. 2. Three-phonon and four-phonon RTA scattering rates of ZA phonons in graphene with varying tensile strain (2%, 4%, and 6%) at 300 and 1000 K, respectively.

atoms, volume, and temperature) realized using the Nosé-Hoover chain thermostat. Secondly, we performed a production run within the *NVT* ensemble for 8 ns, recording and displaying the average heat current per 1000 steps. The time step was set as 1.0 fs. For each system, eight independent similations were performed to get the avaraged thermal conductivity. The HNEMD method was implemented in the Graphics Processing Units Molecular Dynamics (GPUMD) package [52,53], using the neuroevolution potential (NEP) [54], which is a type of machine learning potential based on neural networks.

III. RESULTS AND DISCUSSION

We start by looking into the contribution of thermal conductivity by ZA phonons, κ^{ZA}, in graphene with a tensile strain, which has been shown to dominate the convergence of its κ [13–16]. Figure 1 shows the κ^{ZA} at 300 and 1000 K with respect to the **q**-point mesh calculated using the RTA approach by considering both three- and four-phonon scattering (κ_{3+4}), in comparison with the case that only three-phonon scattering is included (κ_3). The maximum **q**-point mesh for calculating κ_3 and κ_{3+4} using SHENGBTE [38,44] directly is $240 \times 240 \times 1$ and $60 \times 60 \times 1$, respectively. The κ^{ZA} increases almost linearly with **q**-point mesh when only the three-phonon process is considered, which is consistent with the previous work [15,16]. In sharp contrast, after considering the four-phonon process, the κ of graphene with tensile strain is strongly suppressed and shows a convergent trend towards a finite value as the **q**-point mesh increases, especially for the results at 1000 K.

The observation is that the κ of strained graphene diverges within the three-phonon scattering framework, which is consistent with the PBTE calculations by Kuang *et al.* [16]. This phenomenon has been attributed to the frequency dependence of the phonon scattering rates (τ^{-1}) of the long-wavelength ZA phonons, $\tau_3^{-1} \propto \omega^{\beta}$. Specifically, the mode contribution of long-wavelength ZA phonons to thermal conductivity is demonstrated to be proportional to $N^{\beta-2}$, where N represents the grid number of an exceptionally dense mesh. These results revealed that the total κ is convergent only when β is smaller than 2. Kuang *et al.* [16] proved that β will be greater than 2 in graphene under tensile strain when only three-phonon scattering is considered, resulting in a divergent κ.

To understand the difference between the convergence behavior of κ_3 and κ_{3+4}, in Fig. 2, we plot the ZA modal scattering rates for three-phonon τ_3^{-1} and four-phonon τ_4^{-1} processes at 300 and 1000 K calculated by RTA for graphene with strain $\varepsilon = 2\%$, 4%, and 6%, respectively. The scattering rates for $\varepsilon = 8\%$ are shown in Fig. 5 in the Appendix. Similarly, we observe $\beta > 2$ for τ_3^{-1} of long-wavelength ZA phonons in graphene with different tensile strains, which agrees well with the previous work [16]. Differently, in the case of four-phonon scattering rates for ZA phonons with long wavelengths, β is consistently smaller than 2. As a result, four-phonon interaction dominates the frequency dependence of long-wavelength ZA phonons below a critical frequency. This leads to the convergence of the κ of graphene under tensile strain. The critical frequency typically falls below ~0.4 THz within the current strain range at 300 K, but it increases at elevated temperatures. For instance, for graphene with 4% strain, the critical frequency increases from 0.27 to 0.74 THz as the temperature increases from 300 to 1000 K. This results from the distinct temperature dependences of three- and four-phonon scattering rates at the long-wavelength limit, at which the former varies with T while the latter varies with T^2 [55].

Now we examine how tensile strain affects the frequency dependencies of the phonon scattering rate for long-wavelength ZA modes. As shown in Fig. 2, the three-phonon scattering rate shows a more pronounced frequency dependence as strain increases at both 300 and 1000 K. To be more precise, the exponent β increases from 2.43 to 2.81 as the tensile strain rises from 2% to 8% at 300 K. With increasing strain, the β value approaches 3, the analytic long-wavelength limit of the frequency dependence of dominant three-phonon processes involving ZA modes [ZA + ZA → TA (LA)] [13]. Despite the notable change in phonon scattering rates, the *aaa* processes involving three acoustic phonons remain the dominant three-phonon channel for ZA modes in graphene after tensile strains are applied, as shown in Fig. 6 in the Appendix. In contrast, the frequency dependence of the τ_4^{-1} mostly decreases with increasing strain. Taking the results at 300 K as an example, the frequency dependence of the τ_4^{-1} follows $\omega^{1.54}$ in unstrained graphene and substantially decreases from $\omega^{1.18}$ to $\omega^{0.58}$ as the strain increases from 2% to 6%, then slightly increases to $\omega^{0.61}$ as the strain increases to 8%. Similarly, the four-phonon scattering rates of ZA modes at low frequencies are dominated by the *aaaa* processes involving four acoustic phonons in both unstrained and strained graphene, as shown in Fig. 7 in the Appendix. Specifically, the frequency dependence of τ_4^{-1} contributed by the *aaaa* processes is much weaker than that of other scattering channels for ZA modes at low frequencies in strained graphene. Taking $\varepsilon = 6\%$ as an example, the τ_4^{-1} of the *aaaa* processes follows $\omega^{0.49}$, which is much weaker than that of other channels $\omega^{\beta}(\beta \geqslant 0.99)$ at 1000 K [Fig. 7(b)].

The notable variation of the phonon scattering rates mainly arises from the hardening of the ZA branch (Fig. 8 in the Appendix) and the modification of anharmonic IFCs induced by the tensile strain. On one hand, because the hardening of the ZA branch due to tensile strain becomes weaker as frequency increases, the reduction of the phonon population becomes less at higher frequencies. Therefore, the phonon scattering rates of low-frequency modes are more strongly suppressed as compared to high-frequency modes, leading to enhanced frequency dependence of phonon scattering rates for both three-phonon and four-phonon processes. On the other hand, increasing strain changes the magnitude of the anharmonic IFCs and thus modifies scattering rates, which can implicitly affect the frequency of phonon scattering rates. In general, the magnitude of the third-order IFCs decreases with increasing strain and results in an overall reduction of τ_3^{-1} for all phonon modes, which is expected to have little effect on its frequency dependence. Therefore, the hardening of the ZA phonon branch mainly accounts for the enhanced frequency dependence of τ_3^{-1} at low frequency. The opposite trend observed for τ_4^{-1} indicates that the modification of the fourth-order IFCs dominates over the hardening of the ZA phonon branch in determining its frequency dependence.

Due to the limitation of current computing capability, it is prohibitive to conduct the 3ph+4ph calculation directly using a **q**-point mesh much larger than 60 × 60 × 1. Therefore, we estimated the converged value of $\kappa_{3+4}^{\mathrm{ZA}}$ under the RTA level by approximating the contribution of ZA phonons in the long-wavelength limit using inputs obtained from SHENGBTE [38,44] (see Sec. IIC for calculation details). The convergent $\kappa_{3+4}^{\mathrm{ZA},\infty}$ at 300 K is estimated to be 555, 821, and 1217 W m^{-1} K^{-1} for $\varepsilon = 2\%$, 4%, and 6%, respectively. Because of the important contribution of long-wavelength ZA phonons, experimentally determining the converged value of $\kappa_{3+4}^{\mathrm{ZA}}$ requires large-size samples. For example, the largest mean free path corresponding to 99% of $\kappa_{3+4}^{\mathrm{ZA},\infty}$ at 300 K is ~16, 0.43, and 0.52 mm for $\varepsilon = 2\%$, 4%, and 6%, respectively, indicating a sample size of millimeter scale. At 1000 K, the corresponding mean free path decreases to ~500, 50, and 46 μm, respectively.

Taking the graphene with 6% strain as an example, we further compare the convergence of κ_{3+4} calculated using the iterative approach and RTA. Specifically, we used three approaches with different accuracy, i.e., RTA, 3ph iteration + 4ph RTA, and the full iterative treatment. We verified our full iterative calculation using unstrained graphene, observing that its κ_{3+4} exhibits a convergence behavior with respect to the **q**-point mesh size (see Fig. 9 in the Appendix) similar to that reported by Han and Ruan [56]. As shown in Fig. 3(a), the magnitude of the κ_{3+4} calculated by the iterative approach is much larger than that by RTA. This discrepancy between the iterative and RTA approach is due to the strong normal processes in graphene [32,34]. We note the magnitude of the κ obtained from the 3ph iteration + 4ph RTA approach is almost 99% of that of the full iterative approach for graphene with 6% tensile strain. Compared to the full iterative method, the underestimation of κ_{3+4} obtained from the 3ph iteration + 4ph RTA approach decreases with increasing strain. For instance, the underestimation decreases from almost 22% to 1% as strain increases from 0 to 8% at 1000 K, which can be attributed to the enhanced four-phonon umklapp scattering of the low-frequency modes as the strain increases, as shown in Fig. 10 in the Appendix. Overall, the underestimation is less than 10% for $\varepsilon \geqslant 1\%$, indicating the four-phonon iteration has negligible influence on the thermal conductivity prediction. The κ obtained from the iterative approach converges relatively faster than that from RTA, as shown in Fig. 3(b).

To further verify the convergence of κ, we calculated the κ of corresponding systems using molecular dynamics (MD) simulations combined with high-quality machine learning potential [50,52,54]. The obtained thermal conductivity in the strained graphene is well converged (see Fig. 11 in the Appendix).

After confirming the convergence of the κ of the graphene with tensile strain, we next evaluate how κ varies with strain. Figure 3(c) shows the κ_{3+4} of graphene at 1000 K as a function of strain calculated using a 60 × 60 × 1 **q**-point mesh under the full iterative approach and that by MD simulations based

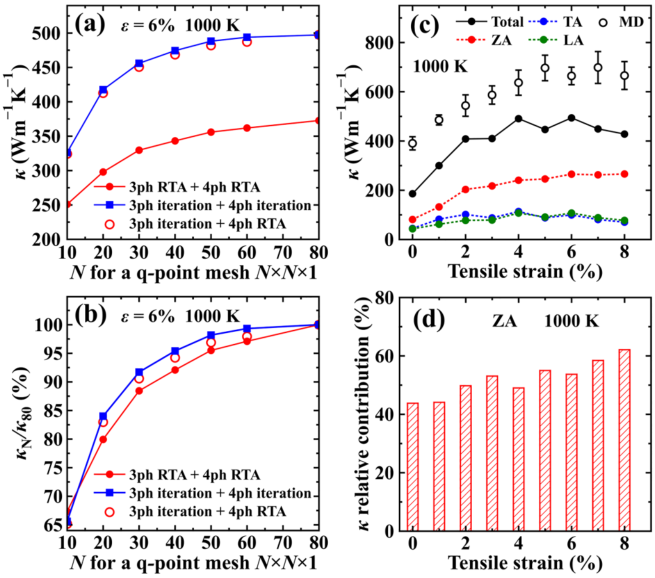

FIG. 3. Convergence of κ of graphene as a function of **q**-point mesh for 6% isotropic tensile strain under full iterative approach at 1000 K (a), in comparison to that under RTA and 3ph iteration + 4ph RTA. (b) The same as (a), but for the κ normalized by that at $N = 80$. (c) The total κ and contribution from different acoustic phonon branches as a function of tensile strain under full iterative approach at 1000 K, along with the MD simulation results with a standard deviation. (d) The relative contribution of κ by ZA phonons under full iterative approach at 1000 K.

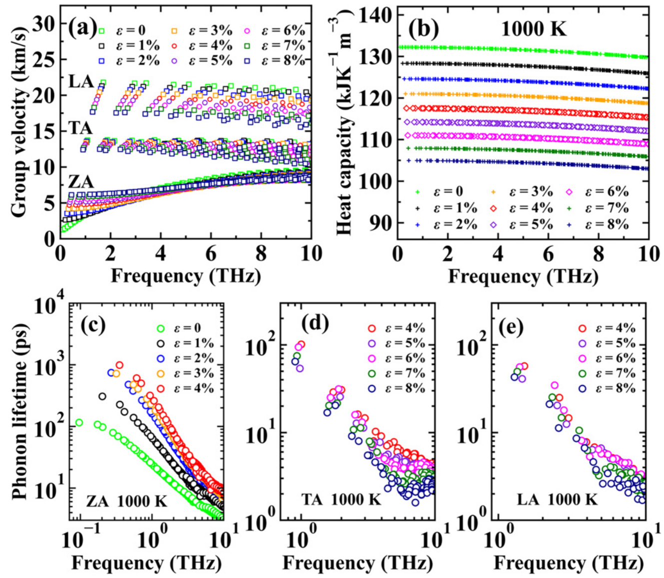

FIG. 4. Strain-dependent group velocity (a), heat capacity (b), phonon lifetime of ZA (c), and that of TA (d) and LA (e) phonons as a function of frequency.

on machine learning potential. Overall, both methods predict a nonmonotonic strain dependence of κ in the strain range $0 \leqslant \varepsilon \leqslant 8\%$. Specifically, as the strain increases, the κ_{3+4} increases for $\varepsilon \leqslant 0.04$ and decreases for $\varepsilon \geqslant 6\%$, while the κ for $\varepsilon = 5\%$ is slightly lower compared to that corresponding to $\varepsilon = 4\%$ and 6%.

To understand the strain dependence of κ_{3+4}, we also plot the κ_{3+4} contributed by each acoustic phonon branch. As is shown in Fig. 3(c), ZA phonons dominate the increase of κ_{3+4} for $\varepsilon < 4\%$, while the TA and LA phonons dominate the reduction of κ_{3+4} for $\varepsilon > 6\%$. We note the $\kappa_{3+4}^{\mathrm{ZA}}$ increases from 81 to 266 W m^{-1} K^{-1} as strain increases from 0 to 8%, which is due to the reduced ZA scattering rates with the increasing strain.

Also, the relative contribution of κ_{3+4} by ZA phonons increases with increasing strain in general, as shown in Fig. 3(d). For example, the relative contribution of κ_{3+4} by ZA phonons at 1000 K increases from 44% to 62% as the strain increases from 0 to 8%. This is because $\kappa_{3+4}^{\mathrm{ZA}}$ increases faster than $\kappa_{3+4}^{\mathrm{TA}}$ and $\kappa_{3+4}^{\mathrm{LA}}$ as strain increases from 0 to 2%, and $\kappa_{3+4}^{\mathrm{ZA}}$ continues to increase while $\kappa_{3+4}^{\mathrm{TA}}$ and $\kappa_{3+4}^{\mathrm{LA}}$ remain almost unchanged as strain increases from 2% to 8%.

To further understand the nonmonotonic behavior of the κ_{3+4} for $0 \leqslant \varepsilon \leqslant 8\%$, in Fig. 4, we plot the group velocity, heat capacity, and the phonon lifetime at 1000 K, which essentially determine the behavior of thermal conductivity. When a strain is applied, the group velocity and heat capacity change due to the shift of phonon branches while the phonon lifetime is affected by the variation of both harmonic and anharmonic IFCs. As the strain increases from 0 to 4%, although the heat capacity decreases, the lifetime and group velocity of the ZA phonon increases, resulting in an increase of the κ_{3+4}. Compared to the κ_{3+4} for $\varepsilon = 4\%$ and 6%, the slight reduction of κ_{3+4} for $\varepsilon = 5\%$ is due to the lower phonon lifetime of the TA and LA phonons, as is shown in Figs. 4(d) and 4(e). As the strain increases from 6% to 8%, the group velocities of the acoustic phonons change little while the heat capacity and phonon lifetime of TA and LA phonons decrease a lot, leading to the reduction of κ_{3+4}.

Overall, as strain increases, the group velocities of ZA phonons increase, while those of TA and LA phonons decrease, as is shown in Fig. 4(a). This is because the ZA branch becomes hardened, while TA and LA branches become softened with increasing strain, as shown in Fig. 8 in the Appendix. The heat capacities of ZA modes decrease due to the hardened phonon dispersion and the increased unit cell volume for strained systems with increasing strain. In contrast, the phonon population of TA and LA modes slightly decreases due to the softened phonon dispersion, indicating the decrease of the heat capacities of TA and LA modes is dominated by the increase of the unit cell volume for strained systems. As shown in Fig. 4(c), the phonon lifetime of ZA modes increases with increasing strain, which can be attributed to the weakened scattering strength caused by the strain-induced linearization of the ZA branch.

As presented above, the divergence of the κ of 2D materials depends on the magnitude of β. Because of tensile strain, the magnitude of β for three-phonon scattering becomes larger than 2 and thus makes a divergent κ in graphene. After taking into account the four-phonon scattering, κ in the strained graphene becomes convergent because the value of β in τ_4^{-1} is smaller than 2. Similarly, the divergent κ within a three-phonon framework was also observed in strained silicene [57], germanene, stanine [58], and h-BN [15], indicating β is larger than 2 in these 2D materials. One may expect four-phonon scattering to have a similar influence on the magnitude of β and result in convergent κ in other 2D materials with tensile strain. It should be pointed out that the divergence of κ can be determined by different acoustic branches. For example, the divergent κ of silicene was due to LA phonons as compared to ZA phonons in graphene [59]. Therefore, how four-phonon scattering affects the thermal conductivity of strained 2D materials is a fascinating and complex issue, which needs to be further explored.

IV. CONCLUSIONS

In summary, we have investigated the thermal conductivity of monolayer graphene with varying tensile strains up to 8% by solving the exact solution of the linearized PBTE in combination with machine learning assisted molecular dynamics simulations. Our first-principles results illustrate that a convergent thermal conductivity in strained graphene can be obtained, provided that four-phonon interactions are incorporated into the calculations. This stems from the dominance of the four-phonon scattering rate of ZA modes in the thermal transport of strained graphene, coupled with its significantly weaker frequency dependency ($\tau_4^{-1} \propto \omega^{\beta}$ with $\beta < 2$) compared to the three-phonon scattering case ($\tau_3^{-1} \propto \omega^{\beta}$ with $\beta > 2$). Furthermore, we observe a nonmonotonic trend in thermal conductivity with varying tensile strains. Within the range of 0–4%, strain leads to an enhancement of thermal conductivity owing to the increased phonon lifetime and group velocity of the dominant long-wavelength ZA modes. As strain continues to increase, in contrast, the thermal conductivity decreases, which can be attributed to the reduction of heat capacity and phonon lifetime for the in-plane acoustic modes.

ACKNOWLEDGMENTS

We thank Xiulin Ruan and Lucas Lindsay for their helpful discussions. We acknowledge support from the Excellent Young Scientists Fund (Overseas) of Shandong Province (Grant No. 2022HWYQ-091), the Taishan Scholars Program of Shandong Province, the Natural Science Foundation Shandong Province (Grant No. ZR2022MA011), the Initiative Research Fund of Shandong Institute of Advanced Technology, and the National Natural Science Foundation of China (Grant No. 52076089). This work used the research computing facilities at Shandong Institute of Advanced Technology.

APPENDIX

See Figs. 5–11.

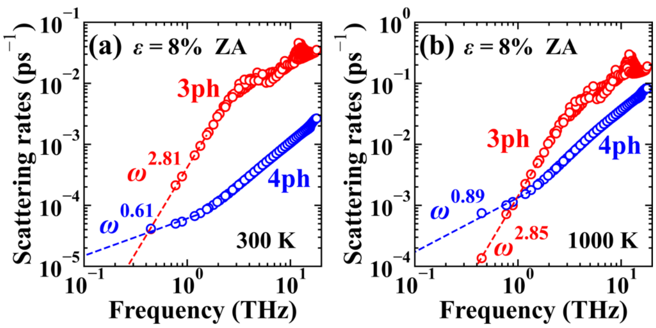

FIG. 5. Three-phonon and four-phonon RTA scattering rates of ZA phonons in graphene with a tensile strain $\varepsilon = 8\%$ at (a) 300 and (b) 1000 K, respectively.

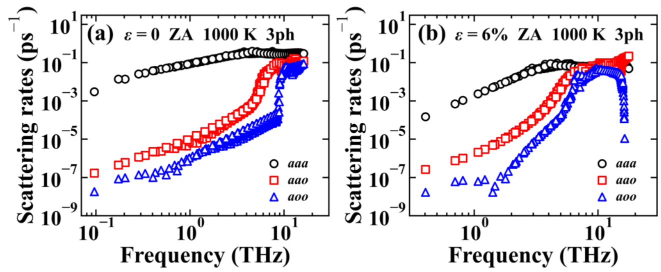

FIG. 6. Three-phonon scattering rates of ZA modes contributed by different scattering channels at 1000 K in graphene with $\varepsilon = 0$ (a) and $\varepsilon = 6\%$ (b), respectively.

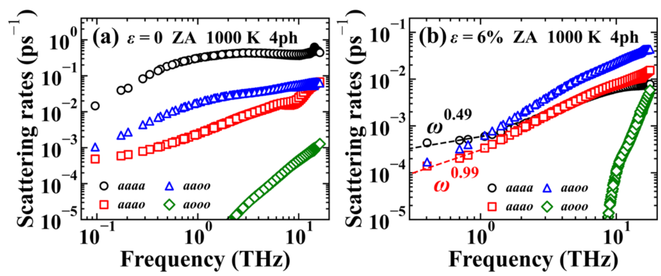

FIG. 7. Four-phonon scattering rates of ZA modes contributed by different scattering channels at 1000 K in graphene with $\varepsilon = 0$ (a) and $\varepsilon = 6\%$ (b), respectively.

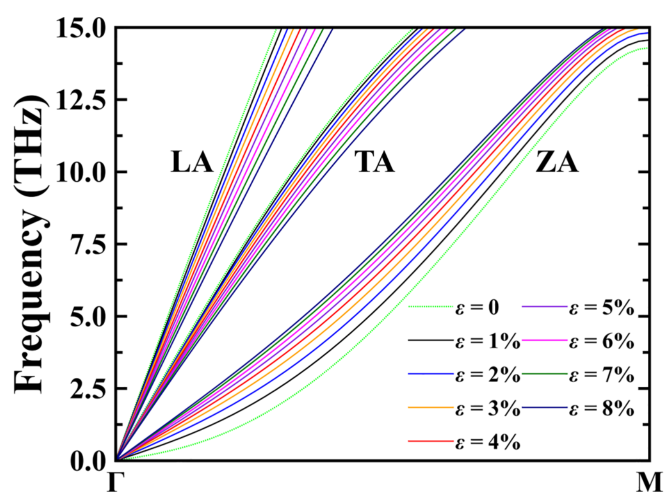

FIG. 8. The calculated acoustic phonon dispersion around $\mathbf{\Gamma}$ point in the direction from $\mathbf{\Gamma}$ to M for graphene with varying tensile strains.

Figure 8 shows the strain-dependent phonon dispersion for the acoustic modes around the Γ point in the direction from Γ to M. The ZA phonons become progressively hardened while the TA and LA phonons become softened with increasing tensile strain. The change of the phonon frequency depends on the mode-specific Grüneisen parameter, which is defined as $\gamma_\lambda = -(\Delta\omega_\lambda/\Delta V)/(\omega_\lambda/V)$, where V is the crystal volume [35].

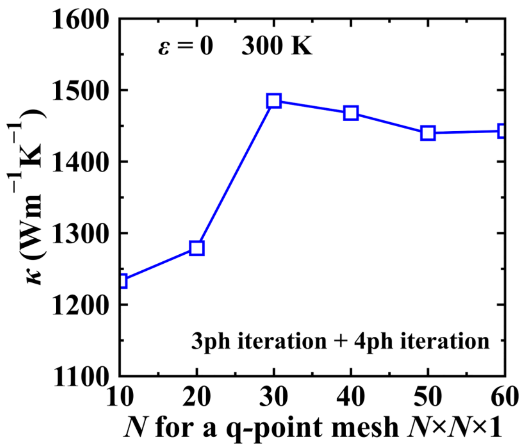

FIG. 9. Convergence of κ of unstrained graphene as a function of **q**-point mesh under full iterative approach at 300 K.

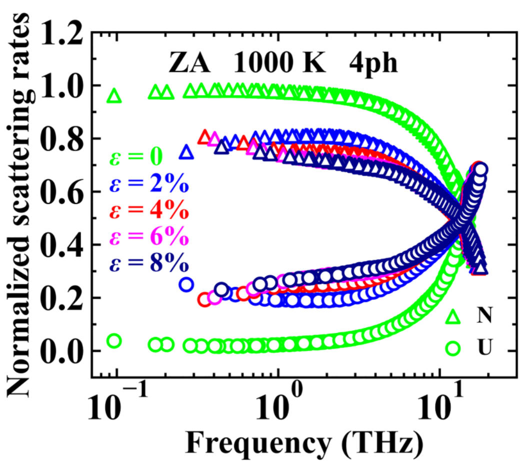

FIG. 10. The four-phonon scattering rates contributed by the normal and umklapp processes normalized by the total four-phonon scattering rates. Unstrained graphene and four tensile strains (2%, 4%, 6%, and 8%) are considered here.

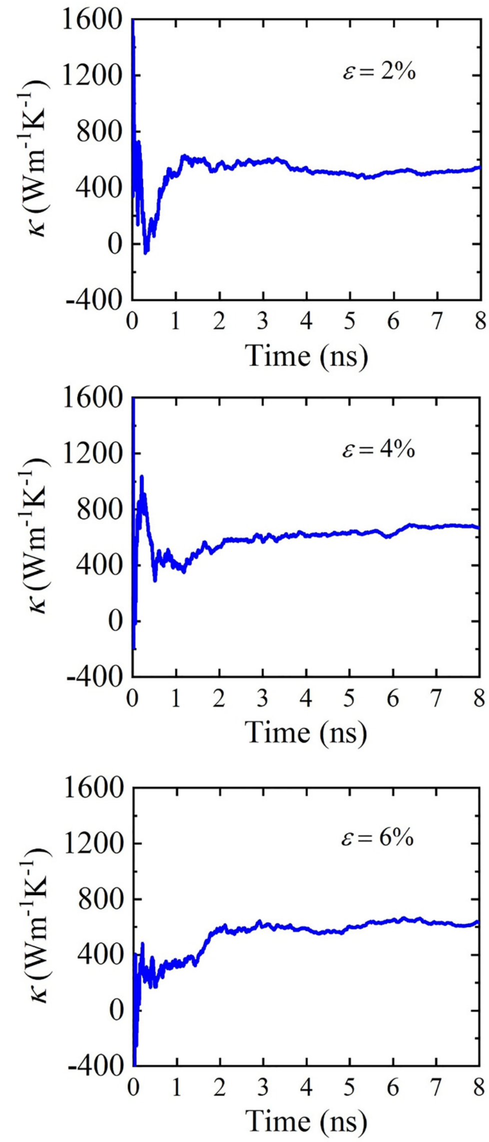

FIG. 11. Running thermal conductivity as a function of time in the nonequilibrium production stage of the HNEMD simulation for graphene with a tensile strain of 2%, 4%, and 6% at 1000 K, respectively. The thermal conductivity is well converged.

[1] S. Yang, Y. Chen, and C. Jiang, Strain engineering of two-dimensional materials: Methods, properties, and applications, InfoMat **3**, 397 (2021).

[2] S. Deng, A. V. Sumant, and V. Berry, Strain engineering in two-dimensional nanomaterials beyond graphene, Nano Today **22**, 14 (2018).

[3] X. Gu, Y. Wei, X. Yin, B. Li, and R. Yang, Colloquium: Phononic thermal properties of two-dimensional materials, Rev. Mod. Phys. **90**, 041002 (2018).

[4] M. Huang, H. Yan, C. Chen, D. Song, T. F. Heinz, and J. Hone, Phonon softening and crystallographic orientation of strained graphene studied by Raman spectroscopy, Proc. Natl. Acad. Sci. USA **106**, 7304 (2009).

[5] S. Shen, A. Henry, J. Tong, R. Zheng, and G. Chen, Polyethylene nanofibres with very high thermal conductivities, Nat. Nanotechnol. **5**, 251 (2010).

[6] Y. Xu, D. Kraemer, B. Song, Z. Jiang, J. Zhou, J. Loomis, J. Wang, M. Li, H. Ghasemi, X. Huang, X. Li, and G. Chen, Nanostructured polymer films with metal-like thermal conductivity, Nat. Commun. **10**, 1771 (2019).

[7] S. Li, Z. Qin, H. Wu, M. Li, M. Kunz, A. Alatas, A. Kavner, and Y. Hu, Anomalous thermal transport under high pressure in boron arsenide, Nature (London) **612**, 459 (2022).

[8] X. Meng, T. Pandey, J. Jeong, S. Fu, J. Yang, K. Chen, A. Singh, F. He, X. Xu, J. Zhou, W. P. Hsieh, A. K. Singh, J. F. Lin, and

Y. Wang, Thermal conductivity enhancement in MoS_2 under extreme strain, Phys. Rev. Lett. **122**, 155901 (2019).

[9] Y. Yue, K. Liu, M. Li, and X. Hu, Thermal manipulation of carbon nanotube fiber by mechanical stretching, Carbon **77**, 973 (2014).

[10] D. Gerlich and P. Andersson, Temperature and pressure effects on the thermal conductivity and heat capacity of CsCl, CsBr and CsI, J. Phys. C: Solid State Phys. **15**, 5211 (1982).

[11] W. P. Hsieh, B. Chen, J. Li, P. Keblinski, and D. G. Cahill, Pressure tuning of the thermal conductivity of the layered muscovite crystal, Phys. Rev. B **80**, 180302(R) (2009).

[12] D. A. Dalton, W. P. Hsieh, G. T. Hohensee, D. G. Cahill, and A. F. Goncharov, Effect of mass disorder on the lattice thermal conductivity of MgO periclase under pressure, Sci. Rep. **3**, 2400 (2013).

[13] N. Bonini, J. Garg, and N. Marzari, Acoustic phonon lifetimes and thermal transport in free-standing and strained graphene, Nano Lett. **12**, 2673 (2012).

[14] L. F. C. Pereira and D. Donadio, Divergence of the thermal conductivity in uniaxially strained graphene, Phys. Rev. B **87**, 125424 (2013).

[15] Y. Kuang, L. Lindsay, and B. Huang, Unusual enhancement in intrinsic thermal conductivity of multilayer graphene by tensile strains, Nano Lett. **15**, 6121 (2015).

[16] Y. Kuang, L. Lindsay, S. Shi, X. Wang, and B. Huang, Thermal conductivity of graphene mediated by strain and size, Int. J. Heat Mass Transfer **101**, 772 (2016).

[17] C. Lee, X. Wei, J. W. Kysar, and J. Hone, Measurement of the elastic properties and intrinsic strength of monolayer graphene, Science **321**, 385 (2008).

[18] K. S. Novoselov, A. K. Geim, S. V. Morozov, D. Jiang, Y. Zhang, S. V. Dubonos, I. V. Grigorieva, and A. A. Firsov, Electric field effect in atomically thin carbon films, Science **306**, 666 (2004).

[19] A. A. Balandin, Thermal properties of graphene and nanostructured carbon materials, Nat. Mater. **10**, 569 (2011).

[20] Y. Wang, A. Vallabhaneni, J. Hu, B. Qiu, Y. P. Chen, and X. Ruan, Phonon lateral confinement enables thermal rectification in asymmetric single-material nanostructures, Nano Lett. **14**, 592 (2014).

[21] A. A. Balandin, S. Ghosh, W. Bao, I. Calizo, D. Teweldebrhan, F. Miao, and C. N. Lau, Superior thermal conductivity of single-layer graphene, Nano Lett. **8**, 902 (2008).

[22] S. Chen, Q. Wu, C. Mishra, J. Kang, H. Zhang, K. Cho, W. Cai, A. A. Balandin, and R. S. Ruoff, Thermal conductivity of isotopically modified graphene, Nat. Mater. **11**, 203 (2012).

[23] X. Xu, L. F. Pereira, Y. Wang, J. Wu, K. Zhang, X. Zhao, S. Bae, C. Tinh Bui, R. Xie, J. T. Thong, B. H. Hong, K. P. Loh, D. Donadio, B. Li, and B. Ozyilmaz, Length-dependent thermal conductivity in suspended single-layer graphene, Nat. Commun. **5**, 3689 (2014).

[24] E. P. Randviir, D. A. C. Brownson, and C. E. Banks, A decade of graphene research: Production, applications and outlook, Mater. Today **17**, 426 (2014).

[25] M. Guo, Y. Qian, H. Qi, K. Bi, and Y. Chen, Experimental measurements on the thermal conductivity of strained monolayer graphene, Carbon **157**, 185 (2020).

[26] K. Nakagawa, K. Satoh, S. Murakami, K. Takei, S. Akita, and T. Arie, Controlling the thermal conductivity of multilayer graphene by strain, Sci. Rep. **11**, 19533 (2021).

[27] X. Li, K. Maute, M. L. Dunn, and R. Yang, Strain effects on the thermal conductivity of nanostructures, Phys. Rev. B **81**, 245318 (2010).

[28] L. Lindsay, W. Li, J. Carrete, N. Mingo, D. A. Broido, and T. L. Reinecke, Phonon thermal transport in strained and unstrained graphene from first principles, Phys. Rev. B **89**, 155426 (2014).

[29] G. Fugallo, A. Cepellotti, L. Paulatto, M. Lazzeri, N. Marzari, and F. Mauri, Thermal conductivity of graphene and graphite: Collective excitations and mean free paths, Nano Lett. **14**, 6109 (2014).

[30] P. G. Klemens, Theory of thermal conduction in thin ceramic films, Int. J. Thermophys. **22**, 265 (2001).

[31] P. G. Klemens and D. F. Pedraza, Thermal conductivity of graphite in the basal plane, Carbon **32**, 735 (1994).

[32] L. Lindsay, D. A. Broido, and N. Mingo, Flexural phonons and thermal transport in graphene, Phys. Rev. B **82**, 115427 (2010).

[33] J. H. Seol, I. Jo, A. L. Moore, L. Lindsay, Z. H. Aitken, M. T. Pettes, X. Li, Z. Yao, R. Huang, D. Broido, N. Mingo, R. S. Ruoff, and L. Shi, Two-dimensional phonon transport in supported graphene, Science **328**, 213 (2010).

[34] T. Feng and X. Ruan, Four-phonon scattering reduces intrinsic thermal conductivity of graphene and the contributions from flexural phonons, Phys. Rev. B **97**, 045202 (2018).

[35] X. Gu, Z. Fan, H. Bao, and C. Y. Zhao, Revisiting phonon-phonon scattering in single-layer graphene, Phys. Rev. B **100**, 064306 (2019).

[36] M. Omini and A. Sparavigna, An iterative approach to the phonon Boltzmann equation in the theory of thermal conductivity, Phys. B (Amsterdam) **212**, 101 (1995).

[37] M. Omini and A. Sparavigna, Beyond the isotropic-model approximation in the theory of thermal conductivity, Phys. Rev. B **53**, 9064 (1996).

[38] W. Li, J. Carrete, N. A. Katcho, and N. Mingo, ShengBTE: A solver of the Boltzmann transport equation for phonons, Comput. Phys. Commun. **185**, 1747 (2014).

[39] S. Baroni, S. de Gironcoli, A. Dal Corso, and P. Giannozzi, Phonons and related crystal properties from density-functional perturbation theory, Rev. Mod. Phys. **73**, 515 (2001).

[40] G. Kresse and J. Furthmuller, Efficient iterative schemes for *ab initio* total-energy calculations using a plane-wave basis set, Phys. Rev. B **54**, 11169 (1996).

[41] P. E. Blöchl, Projector augmented-wave method, Phys. Rev. B **50**, 17953 (1994).

[42] J. P. Perdew and A. Zunger, Self-interaction correction to density-functional approximations for many-electron systems, Phys. Rev. B **23**, 5048 (1981).

[43] A. Togo, F. Oba, and I. Tanaka, First-principles calculations of the ferroelastic transition between rutile-type and $CaCl_2$-type SiO_2 at high pressures, Phys. Rev. B **78**, 134106 (2008).

[44] Z. Han, X. Yang, W. Li, T. Feng, and X. Ruan, FourPhonon: An extension module to ShengBTE for computing four-phonon scattering rates and thermal conductivity, Comput. Phys. Commun. **270**, 108179 (2022).

[45] N. R. Werthamer, Self-consistent phonon formulation of anharmonic lattice dynamics, Phys. Rev. B **1**, 572 (1970).

[46] T. Tadano and S. Tsuneyuki, Self-consistent phonon calculations of lattice dynamical properties in cubic $SrTiO_3$ with first-principles anharmonic force constants, Phys. Rev. B **92**, 054301 (2015).

[47] J. Zheng, D. Shi, Y. Yang, C. Lin, H. Huang, R. Guo, and B. Huang, Anharmonicity-induced phonon hardening and phonon transport enhancement in crystalline perovskite $BaZrO_3$, Phys. Rev. B **105**, 224303 (2022).

[48] J. Zheng, D. Shi, S. Liu, Y. Yang, C. Lin, Z. Chang, R. Guo, and B. Huang, Effects of high-order anharmonicity on anomalous lattice dynamics and thermal transport in fully filled skutterudite $YbFe_4Sb_{12}$, Phys. Rev. Mater. **6**, 093801 (2022).

[49] D. J. Evans, Homogeneous NEMD algorithm for thermal conductivity—application of non-canonical linear response theory, Phys. Lett. A **91**, 457 (1982).

[50] Z. Fan, H. Dong, A. Harju, and T. Ala Nissila, Homogeneous nonequilibrium molecular dynamics method for heat transport and spectral decomposition with many-body potentials, Phys. Rev. B **99**, 064308 (2019).

[51] Z. Fan, L. F. C. Pereira, H. Q. Wang, J. C. Zheng, D. Donadio, and A. Harju, Force and heat current formulas for many-body potentials in molecular dynamics simulations with applications to thermal conductivity calculations, Phys. Rev. B **92**, 094301 (2015).

[52] Z. Fan, T. Siro, and A. Harju, Accelerated molecular dynamics force evaluation on graphics processing units for thermal conductivity calculations, Comput. Phys. Commun. **184**, 1414 (2013).

[53] Z. Fan, W. Chen, V. Vierimaa, and A. Harju, Efficient molecular dynamics simulations with many-body potentials on graphics processing units, Comput. Phys. Commun. **218**, 10 (2017).

[54] Z. Fan, Y. Xiao, Y. Wang, P. Ying, S. Chen, and H. Dong, Combining linear-scaling quantum transport and machine-learning molecular dynamics to study thermal and electronic transports in complex materials, arXiv:2310.15314.

[55] T. Feng, L. Lindsay, and X. Ruan, Four-phonon scattering significantly reduces intrinsic thermal conductivity of solids, Phys. Rev. B **96**, 161201(R) (2017).

[56] Z. Han and X. Ruan, Thermal conductivity of monolayer graphene: Convergent and lower than diamond, Phys. Rev. B **108**, L121412 (2023).

[57] H. Xie, T. Ouyang, É. Germaneau, G. Qin, M. Hu, and H. Bao, Large tunability of lattice thermal conductivity of monolayer silicene via mechanical strain, Phys. Rev. B **93**, 075404 (2016).

[58] Y. D. Kuang, L. Lindsay, S. Q. Shi, and G. P. Zheng, Tensile strains give rise to strong size effects for thermal conductivities of silicene, germanene and stanene, Nanoscale **8**, 3760 (2016).

[59] X. Gu and R. Yang, First-principles prediction of phononic thermal conductivity of silicene: A comparison with graphene, J. Appl. Phys. **117**, 025102 (2015).